Engineering Structures 274 (2023) 115159

Contents lists available at ScienceDirect

Engineering Structures

journal homepage: www.elsevier.com/locate/engstruct

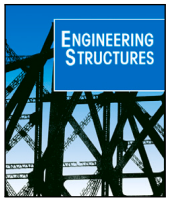

Probabilistic friction model for aluminium–steel Asymmetric Friction Connections (AFC)

Angelo Aloisio [a,d,*], Alessandro Contento [b], Francesco Boggian [c,d], Roberto Tomasi [d]

[a] Department of Civil, Construction-Architecture and Environmental Engineering, University of L'Aquila, L'Aquila, Italy
[b] College of Civil Engineering, Fuzhou University, Fuzhou, China
[c] Department of Civil, Environmental and Mechanical Engineering, University of Trento, Trento, Italy
[d] Faculty of Science and Technology, Norwegian University of Life Sciences, Ås, Norway

ARTICLE INFO

Keywords:
Friction dampers
Probabilistic model
Bayesian calibration
Seismic protection
Structural design

ABSTRACT

Multiple physical variables potentially affect the friction coefficient of Asymmetric Friction Connections (AFC). This paper discusses the cyclic response of a class of AFC subjected to repeated load protocols. Two phenomena are observed. First, the friction coefficient, initially higher due to wear phenomena and moment-axial force-shear force interaction, stabilizes after multiple cycles. Second, the test repetitions on the same specimen show that the friction coefficient at the beginning of the loading protocol is higher than that observed at the end of the antecedent load protocol. The experimental data prove that the dissipated energy during the current load test, temperature, and the specimen's history affect the friction coefficient. This paper presents two probabilistic friction models calibrated using a Bayesian approach. The first engineering-oriented model is dependent on the dissipated hysteretic energy. The second includes the measured temperature as a model regressor to estimate its possible role in the response. The proposed probabilistic models can be used to predict with satisfactory accuracy the friction coefficient in Coulomb-like hysteresis models of AFCs.

1. Introduction

Among hysteretic devices, friction dampers have been gaining more attention in the last few years. These dampers dissipate seismic energy by mechanical damping through sliding friction with the primary "braking rather than breaking" principle [1]. There is a wide range of applications of friction dampers, from civil to mechanical and avionic engineering [2,3]. However, there are still a few attempts to use friction dampers for seismic retrofitting civil structures.

Venuti 1976 [4] and Pall et al. in 1980 [1] were the first to add friction devices as additional damping sources in civil structures. The Limited Slip Bolt (LSB), evolved to the Pall Frictional Damper (PFD), exhibited stable, almost rectangular hysteresis cycles [5,6]. PFD is conceived for X- and K-bracings. Its worldwide success has confirmed the merits of the PFD. Multiple applications and research papers are proving the value and efficiency of the PFD [7–10]. The main drawbacks of PFD are the relatively low capacity (less than 10 kips), the need for high precision work for its manufacture, and specialized training for the installation process [11,12].

In 1989 Fitzgerald et al. [13] devised a friction connection called the Slotted Bolted Connection (SBC), characterized by a more straightforward design than the PFD. The proposed SBC worked by sliding channel bracing plate over a gusset plate interconnected by high strength bolts with washers (Belleville spring) for adjusting the bolt tension.

There are two main classes of SBC: the Symmetric and Asymmetric friction connection [14,15]. Symmetric Friction Connection (SFC) is a type of SBC that consists of the main plate (with slotted holes), two brass shims, two outer plates, and high strength bolts. Initially proposed by Clifton [16], Asymmetric Friction Connection (AFC) is another type of SBC [17,18]. AFCs consist of steel plates and shim layers clamped by the pre-tensioned bolts, see Fig. 1. AFC is a crucial component of Sliding Hinge Joints (a low damage beam-to-column connection for the Moment Resisting Frame). AFCs installed in SHJ consist of shims, cleat, cap plate, high strength bolts, and bottom flange of the beam. The friction originates from the sliding between (i) beam bottom flange and upper shim and (ii) cleat and lower shim [16].

Initial developments of AFC were based on brass shims [19]. Subsequent studies by Mackinven [20] extended the application to mild steel and aluminium shims. The AFC is simple to build, cost-effective, and capable of dissipating energy under seismic excitation. However, the AFC hysteretic stability highly depends on the mutual hardness between the steel and shim layers. In addition, the stability of the hysteretic performance is affected by the interaction between abrasive

* Corresponding author.
E-mail addresses: angelo.aloisio@nmbu.no, angelo.aloisio1@univaq.it (A. Aloisio).

https://doi.org/10.1016/j.engstruct.2022.115159
Received 14 March 2022; Received in revised form 10 September 2022; Accepted 16 October 2022

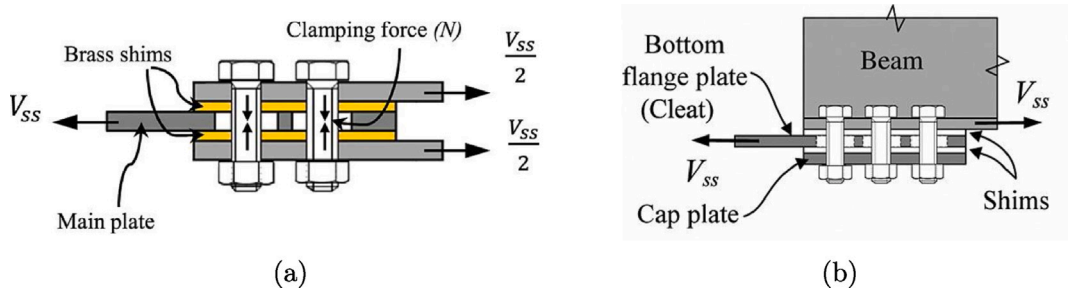

Fig. 1. Illustration of (a) a symmetric friction connection, and (b) asymmetric friction connection.
Source: From [31].

and adhesive wear and friction phenomena. There are several examples of application of AFC connections in real buildings, see [21–23]. A few scholars [24–29] attempted to verify the consequences of wear and friction on AFC in the past years. They found that a stable cyclic behaviour can be achieved if there is a significant difference in the mutual hardness of the siding surfaces, i.e. shim layer and steel plates. The similarity in sliding surfaces' hardness causes a significant instability of the hysteresis loop mainly due to the large amount of work-hardened wear particles produced during the sliding mechanism. These particles abrade the sliding surfaces in an irregular pattern, thus exhibiting a wear abrasive mechanism defined by Grigorian and Popov [19] and Khoo et al. [18]. The stability of the hysteresis curve, in the case of non-lubricated sliding surfaces, depends on the initial wear of the shim or steel plates. For instance, in the case of the shim layer being less hard than the plates, the initial wear increases the roughness of the shim layer. The wear particles generated in this process create lubrication that stabilizes the friction coefficient. Therefore, the wear particles generated in the initial phase are crucial to achieving a stable performance of the AFC. Aluminium shims are among the materials that exhibit the best performance, with the lowest and more stable friction coefficient [30].

Currently the shims to be used in AFC are recommended to be abrasion-resistant, like (high hardness) steel [18,32,33]. Nonetheless, AFCs with high hardness cleat and high hardness shims do not provide specific benefit on the seismic performance [34]. In line with the findings by Ramhormozian et al. [34], the authors observed that softer shim layers (like aluminium) exhibited a more stable response than harder ones (hardox). Therefore, they chose to use aluminium as a shim layer for several reasons, despite multiple pieces of research proposing specific solutions characterized by an excellent hysteretic performance (friction pads [35] using composite or rubber-based [36,37] friction plates, Belleville springs [33] or thermal spray coating materials [38], e.g.). However, compared to composite, rubber-based, or spray materials, aluminium has more stable mechanical properties over time. The authors will attempt to verify the performance improvement due to Belleville springs in future steps. However, at this stage of the e-SAFE project, the authors present the primary and more elementary solution based on aluminium shims that will be a reference in future AFC developments.

There are different typologies of AFCs. The most used and studied is the Sliding Hinge Joint (SHJ). The SHJ is a flexural connection designed to use at the beams' ends in steel moment-resisting frames. It is an AFC where energy is dissipated through sliding in slotted bolted connections in the beam bottom flange [39].

The initial application of friction connections to low-damage moment-resisting joints has been recently extended to pinching-free connections for timber structures [40]. Pinching represents one of the significant weaknesses in timber structures since it is associated with considerable degradation after repeated cycles [41–43].

Loo et al. [44] investigated the possibility of using SFC instead of hold-down for restraining timber shear walls against uplift, to cap the force transmitted to the wall, and reduce inelastic damage. The subsequent experimental campaigns presented in [45,46] established the effectiveness of SFC on reducing the degradation and pinching phenomena typical of timber connections. The following studies presented in [47] pointed to a displacement-based design method for multistorey CLT buildings with friction connections. Next to the findings by Loo et al. [48] studied the response of SFC connected to a CLT panel [49].

Zamani and Quenneville proposed a resilient slip friction connection (RSF) as a hold-down connector for CLT panels [50,51]. The RSF joint is a self-centring friction connection [52–54], which proved to reduce the damage to the CLT panel after multiple cycles.

So far, no AFC was used as a connection system for CLT panels except for the attempts by Boggian et al. [55]. Boggian et al. tested AFCs for a hybrid structural system, the e-CLT technology.

The e-CLT, illustrated in Fig. 2, consists of CLT panels cladding existing RC frames for seismic retrofitting purposes. The CLT panels are connected via AFC to the RC frame. Accordingly, the AFC is triggered if a specif inter-storey drift is attained during the seismic excitation. Aloisio et al. [57] proposed a design method of this structural system based on the optimization of the slip force. This research has been developed within the Horizon 2020 research project e-SAFE (Energy and Seismic AFfordable rEnovation solutions): applying Asymmetric Friction Connection (AFC) dampers and CLT panels on existing reinforced concrete structures.

The experimental tests carried out in [55] highlighted the dependence of the friction coefficient on the cumulative energy dissipation. The experimental tests also revealed that both wear and friction contribute to the hysteretic performance of the connection.

The use of dissimilar sliding surfaces and thin plates inserted at both sides leads to a stable, repeatable and predictable hysteretic behaviour. However, AFC strength degrades when AFCs are cyclically loaded. As remarked by [58], this degradation may result from degradation in compressive force over the surfaces as a result of moment – axial force – shear force interaction (MPV interaction), change in the properties in the sliding surfaces [16,59], and/or prying effects [60,61]. The latter two effects depend on the device assembly, design and implementation. There are a few models predicting the strength degradation due to MPV interaction [17].

The earliest MPV model was proposed by Clifton et al. [16], and later improved by Khoo et al. [17], termed the Clifton model and Khoo model. Recently, Golondrino et al. [58] proposed a nonlinear MPV model for assessing AFC strength considering the bolt rotation and the increase in bolt axial tension due to bolt rotation. As shown in [62] through analytical modelling, the AFC bolts are under MVP interaction during stable sliding, causing the conventionally fully tensioned AFC bolts to deform and lose part of their preload. Furthermore, the AFC may be under prying actions that may plasticize the bolts and result in bolt tension loss. However, the mentioned phenomena can be partially reduced using Belleville springs [33,63,64]. Moreover, in addition to the potential initial, short-term, and long-term bolt tension loss, the high clamping force generated by the bolts causes the post-sliding wearing and thickness reduction of AFC plies, determining a further bolt tension drop.

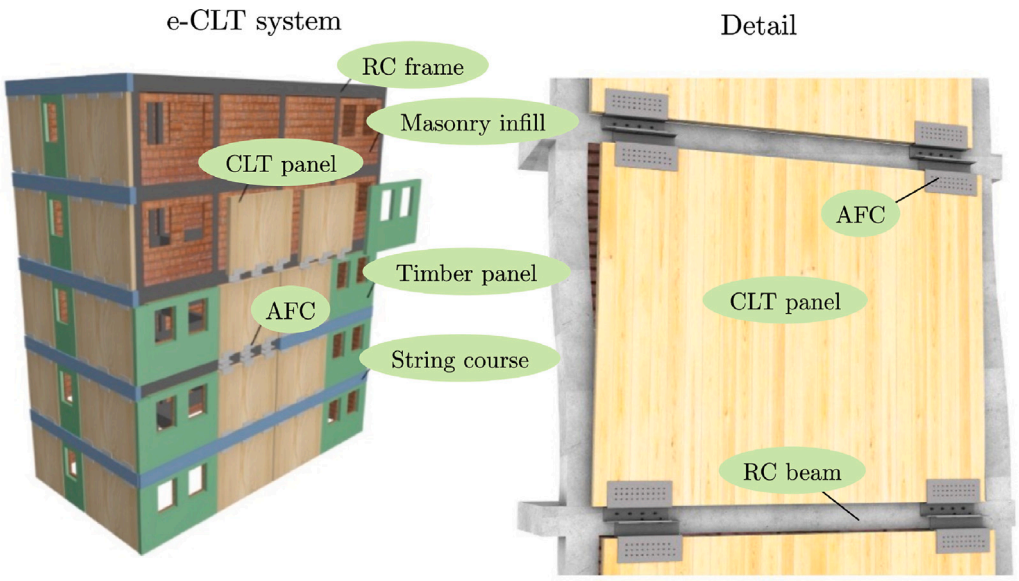

Fig. 2. Illustration of the e-CLT technology after [56].

However, next to mechanics-based formulations, data-driven models can also be used to predict the response of a specific AFC damper, using cyclic test data. The development of data-driven friction models can predict the strength evolution without explicitly considering MPV phenomena. Parameters like the dissipated hysteretic energy and the temperature of the specimen can be used as synthetic regressors of the probabilistic model of friction. This approach, conventional in hysteresis modelling, has been recently followed by [57,65] for simulating the hysteretic response of an AFC in nonlinear dynamic analyses.

To the authors' knowledge, no scholar carried out multiple repetitions of the same load test on the same AFC specimen. The experimental tests carried out by Boggian et al. [55] showed a significant dependence of the AFC strength on the past deformation history of the specimen. Likely, the temperature and the hysteretic energy dissipated during the current and former tests can be effective predictors of the AFC cyclic response.

The experimental data suggested that the friction coefficient depended on both the specimen history and the energy dissipated during the test.

This paper aims at filling the gap of knowledge on the evolution of the friction coefficient after multiple load protocols by developing a probabilistic data-driven friction model dependent on mechanical and thermodynamic parameters. The vast number of data and the uncertainties related to the stability of the experiments supported a Bayesian approach for calibrating a predictive equation of the friction coefficient. Therefore, the objectives and novelties of this research are:

- Multiple repetition of the experimental load tests on AFC specimens.
- Assessment of the contributions of the measured physical variables (e.g., temperature) on the evolution of the friction coefficient.
- Proposal of two probabilistic friction models. The first depends on the dissipated hysteretic energy, while the second also includes the measured temperature as regressor.
- Discussion on the pros and cons of the investigated friction connection and proposal of a possible enhancement of its performance.

The paper has the following structure. The first section presents the experimental tests without in-depth comments and interpretation of the results. The second section is the paper's core. It discusses the experimental data and proposes a functional dependence of the friction coefficient on the generalized number of cycles and the AFC eccentricity. The third section deals with the FE modelling of the friction connection, which highlights the weakness of the proposed AFC connection.

2. Experimental tests

This section presents a detailed description of the tested specimens, the experimental setup and the results in terms of force–displacement and energy–time curves.

2.1. Technological development of the AFC

The tested specimens investigated in this paper originate from a progressive evolution within the e-Safe research project [56]. Therefore, before going through the observed behaviour of the tested AFC, the authors provide a brief introduction to the technological development of the specimens. In detail, the specific AFC configuration is obtained by balancing (i) installation and (ii) structural performance requirements. (i) There is a straightforward installation if the AFC can be screwed to the front of the CLT panel [66]. This solution would also allow minor adjustments to the mutual AFC and CLT panel positions. (ii) The structural requirement consists of reducing the number of bends in the steel profiles and maintaining the eccentricity between the force reaction and the slip forces as small as possible. These aspects were preliminary addressed before the experimental tests from FE analyses [67].

Fig. 3 shows the three solutions tested during the e-Safe project, characterized by different geometry and eccentricity. The AFC in Fig. 3(a) was the first configuration [68], tested in multiple variants, as illustrated in Fig. 4. In the first phase, the specimens' STD showed several critical issues, which led to the development of three variants shown in Fig. 4: STD-R, STD-1H and ALT. In detail, STD, STD-1H STD-R correspond to the category in Fig. 3(a). However, the authors aimed at further reducing the number of bends and eccentricity, which led to specimens ALT, corresponding to the class in Fig. 3(b). However, the ALT, despite having a better structural performance, has several installation drawbacks: back mounting and no yoke for vertical alignment. Therefore, the enhancement of the ALT led to the ALT-AS (Fig. 5) and HYB specimens (Fig. 6), which guarantee a easier installation. The ALT-AS includes an alignment components with vertical slotted holes, permitting a more precise installation of the connection, which

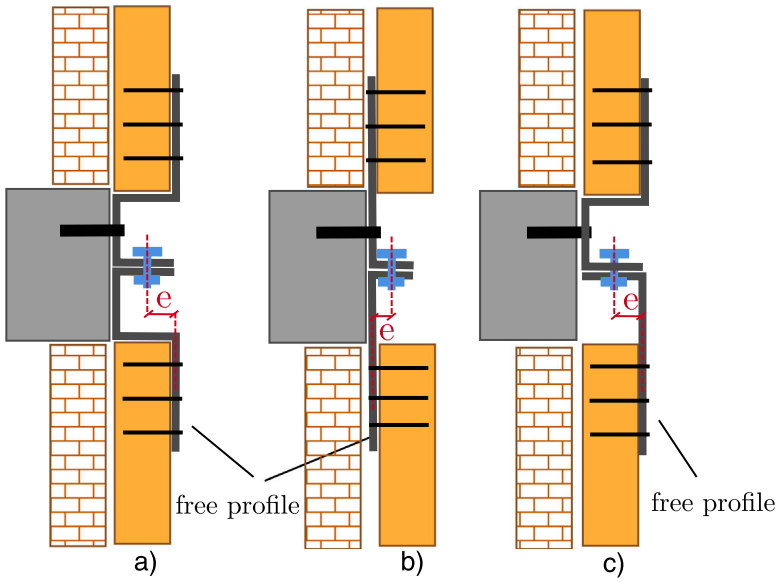

Fig. 3. Illustration of the technological development of the tested AFC throughout the e-SAFE project. The different possible configurations of the free profiles are: (a) front mounting, 3 bends; (b) back mounting, single bend; (c) front mounting, single bend.

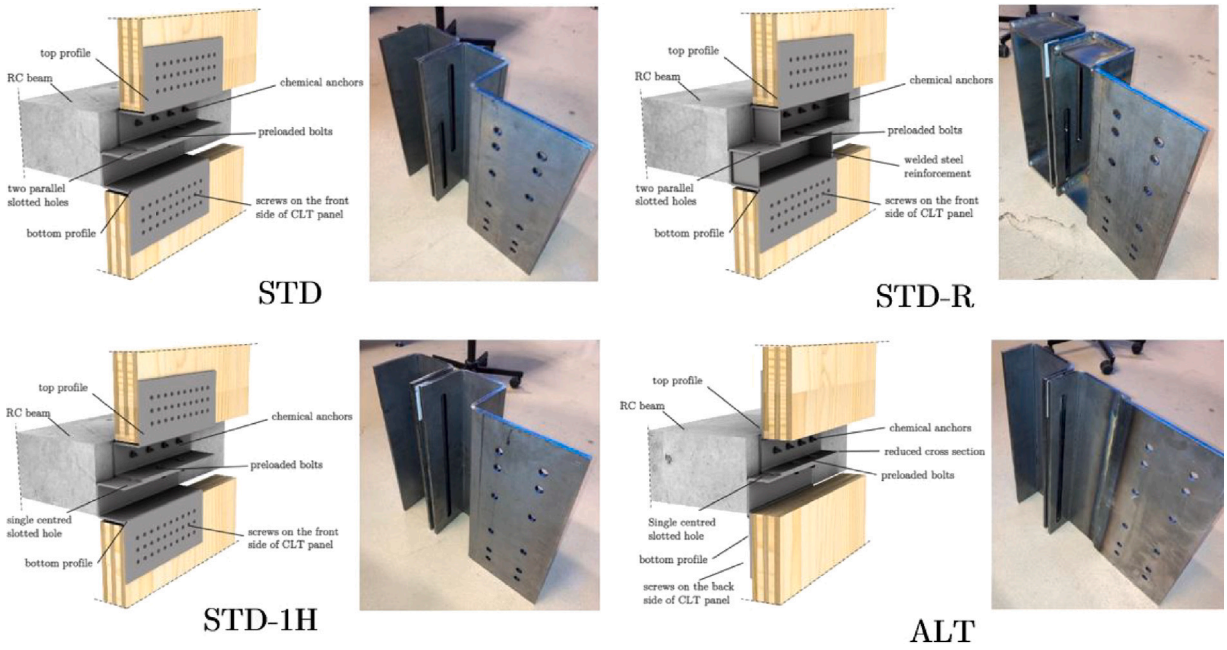

Fig. 4. Illustration of the specimens tested during the first phase.

is valuable, especially in the case of prefabrication. On the other hand, the specimen HYB combines mounting and structural advantages: front screwing of the AFC to the CLT panel and simple L shape. Therefore, the specimens HYB falls in the category of Fig. 3(c). The ALT-AS and HYB both had a satisfactory performance. The extensive experimental characterization focused on the HYB, while the ALT-AS will be deeply investigated in future studies. Therefore, the results and models presented in this paper refer to the HYB specimen, whose geometrical and constructive details are reported in the Appendix in Figs. A.17–A.19.

2.2. Description of the tested specimen

The specimen is named Hybrid after previous AFC designs discussed in the previous paragraphs within the e-SAFE Horizon 2020 research project. The Hybrid specimen (labelled HYB), shown in Fig. 6, attempts to combine the best features of previous designs of the AFC.

The specimen consists of two 8 mm thick cold-bent S355 steel profiles: the anchor profile is connected to the moving head of the press, while the free profile is connected to the CLT panel. The two profiles are clamped together to form an asymmetric friction connection (AFC) by adding an 8 mm steel cap plate and two 2 mm aluminium shim layers. The connection between the two profiles is ensured by high strength M16 10.9 bolts [69], which slide in a 17 mm wide elongated hole. The elongated hole is 100 mm long plus some tolerance and allows for relative sliding between the two profiles. Three different types of HYB specimens were tested, detailed in Table 1. The three AFC typologies had the exact dimensions and shape but exhibited minor geometric variations. Specifically, specimen HYB and HYB_*e* differed in the eccentricity of the friction connection to the timber connection, see

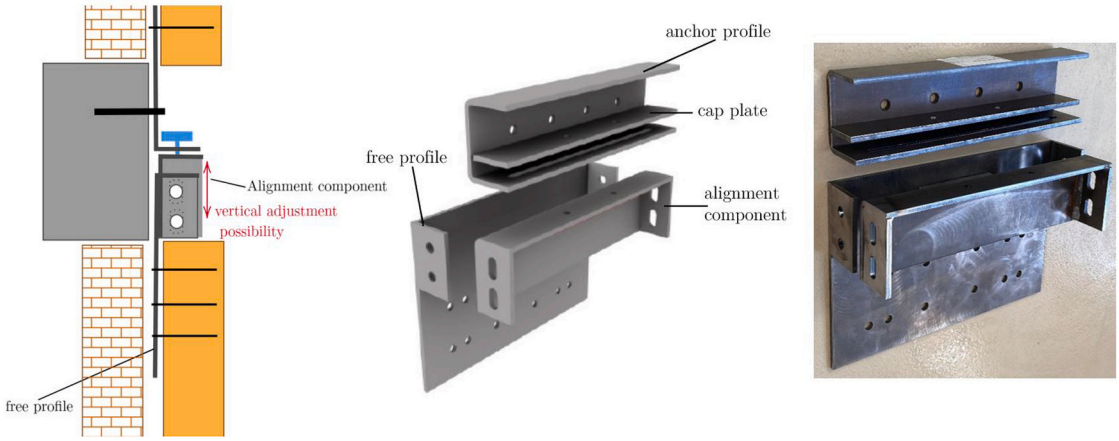

Fig. 5. Illustration of the ALT-AS prototype in the second phase.

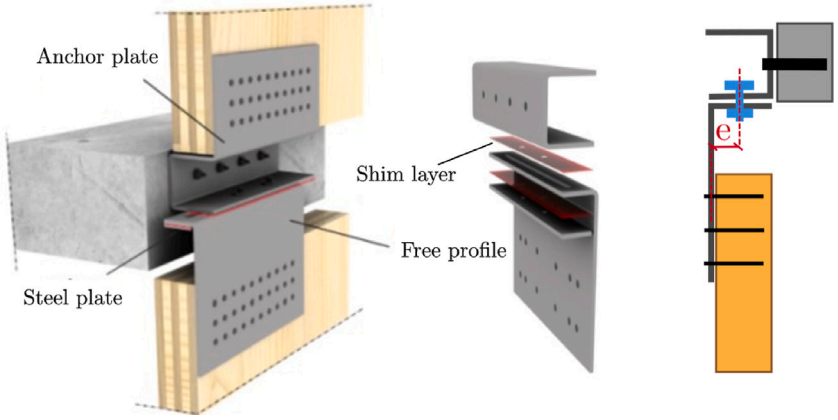

Fig. 6. Illustration of the tested specimen (HYB) with indication of the components and the eccentricity of the AFC.
Source: Modified from [55].

Table 1
Description of the tested specimens with indication of the eccentricity.

Prototype	n	e [mm]	Setup
HYB	3	52.5	With CLT
HYB_e	1	43.5	With CLT
HYB_s	1	52.5	No CLT

Fig. 6. HYB had the elongated hole in the centre of the specimen width, while the elongated hole in HYB_*e* was moved towards the CLT side to observe possible effects of eccentricity variations. The free profile had 33 holes for a screw connection to the CLT panel in both cases. The screws were 10 × 80 mm HBS Plate Evo from Rothoblaas [70]. These specimens were tested following the same setup, with a CLT specimen 100 mm thick, five layers and dimensions 400 × 800 mm. The specimen HYB_s, which had the same eccentricity as the HYB, was used on a slightly different setup: a steel column was used to support the free profile instead of a CLT specimen. Thus the hole pattern was different since bolts substituted the screws. This specimen was made to directly compare the effect of the screw connection on the friction behaviour of the system.

The tested specimens are detailed in Appendix, which shows the executive drawings of the AFCs.

2.3. Experimental setup and load protocol

The tests were carried out in the timber laboratory of the Norwegian University of Life Sciences. Fig. 8 shows the setup comprehensive of the CLT specimen. The CLT specimen is added to the experimental setup in the tests to include the effect of its deformation on the hysteretic response. The fixed profile is rigidly attached to a *T* shape element connected to the actuator of the press machine. The free profile is connected with screws to the CLT panel. The possible rocking response of the CLT specimen is prevented using hold-downs and UPN profiles connected to the base of the press with threaded rods. The hold-down is custom made, with 10 mm thick steel plates, 22 10 × 80 mm screws for the timber and one M30 bolt at the base. The electro-mechanical machine used for the experiments applies a vertical sliding movement, while the force measures are obtained using a load cell with a 1200 kN capacity. The press and an additional wire sensor record the displacement measures of the free profile. A thermocouple measures the temperature on the friction connection, as displayed in Fig. 7. An additional thermocouple was installed on the steel frame of the testing machine to track any possible modification of the temperature of the machine. Thanks to the test rapidity, 2 mm/s, there was no increment of the machine temperature. Therefore, with good approximation, the temperature increment observed in the specimens can be entirely attributed to the friction phenomena since no significant heat transfer occurred during the tests. The setup of the HYB_s specimen does not include CLT specimens to assess the influence of the screw connection [55]. The fixed profile is connected to the press in the same way of the previous tests, while the free profile is rigidly connected to a steel column, part of a frame fixed at the base of the press. The displacement load protocol is applied with a 2 mm/s velocity. The cyclic protocol, following [71], is associated with incremental displacement until reaching the ultimate displacement. In the case of

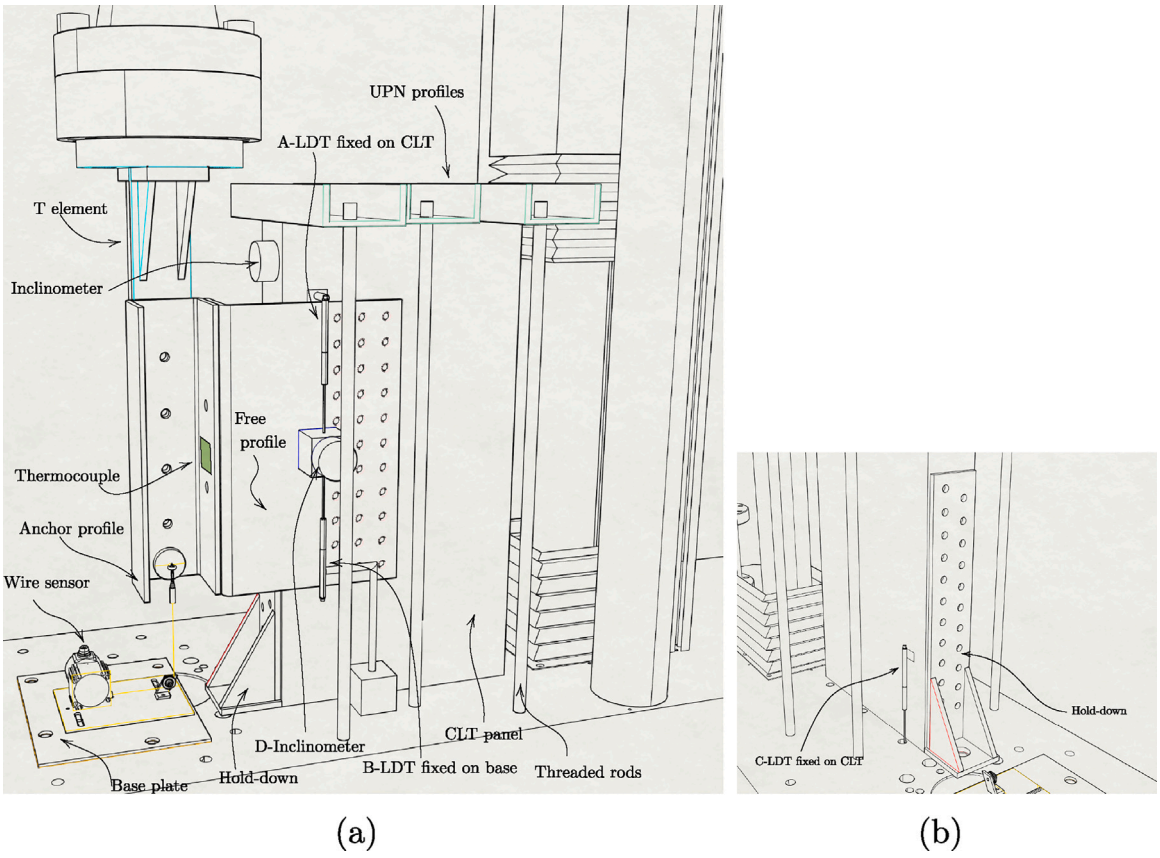

Fig. 7. Parts of the CLT setup. The letters associated with some of the sensors help the readability of the results.

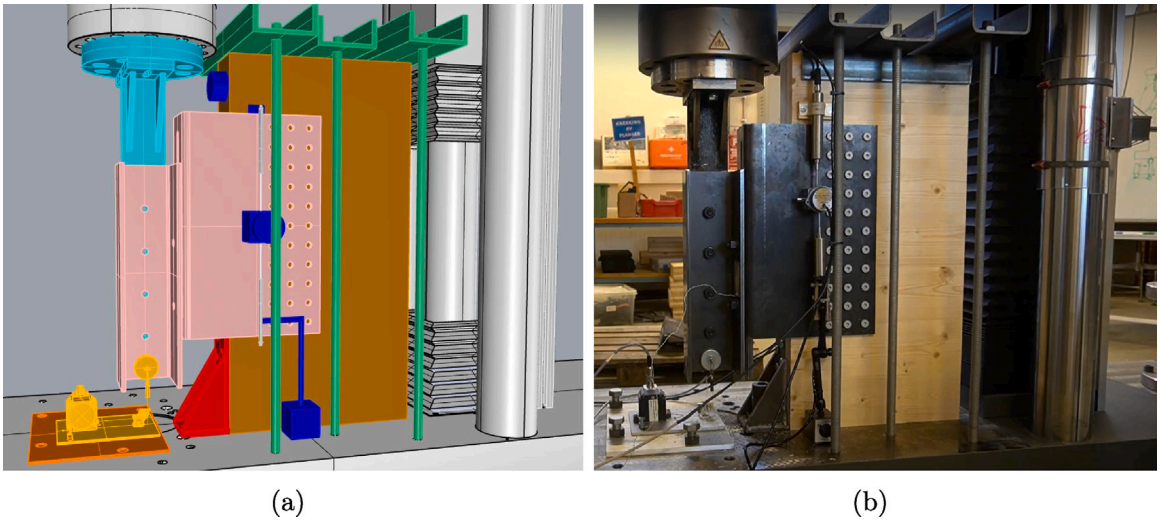

Fig. 8. (a) 3-D simulation of the experimental setup and (b) actual experimental setup.

friction connection, the ultimate displacement can be considered the maximum sliding clearance of the elongated holes, which is 100 mm. Fig. 9 shows the two loading protocols.

The preload was applied using the torque method described in the standard EN1090-2 [72], following the specification of the bolt producer [73]. Specifically, the fixed profile and anchor profile were tightened in two steps using two types of torque wrench depending on the bolt size. One torque wrench ranged from 14 N m to 115 N m and the other from 60 N m to 350 N m. The torque was then measured after each cyclic test with the torque wrench to observe possible prestress losses. Contrarily to what was observed by Qu et al. [74], the authors did not find a significant variation in the prestress, less than 5%. Such a limited variation, better discussed in the following paragraphs, possibly depends on the high constraints provided by the testing machine and the hold-down, which do not allow significant deformations of the profile and force the mutual displacement of the profiles to pure sliding. Consequently, as later assumed, it is reasonable to believe that the variation of the measured slip force depends on temperature variation and wear phenomena. Conversely, the loss in normal forces measured by Qu et al. [74] might be caused by the profile deformation and related MVP interaction. Given the above, the use of loadcells to monitor

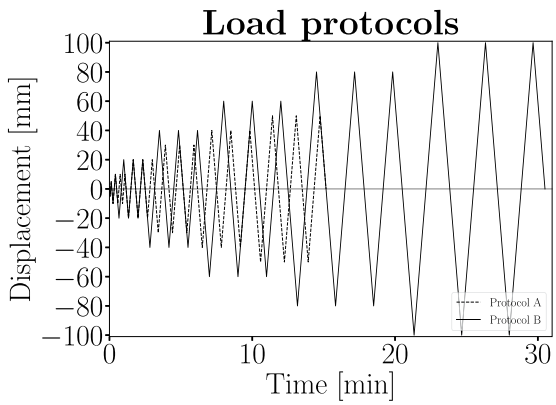

Fig. 9. Load protocols followed in the experimental tests: Protocol A: 1 × 5 mm + 3 × 10–20–30–40–50 mm; 2 mm/s; Protocol B: 1 × 5-10 mm + 3 × 20–40–60–80–100 mm; 2 mm/s.

Table 2
Overview of the experimental tests.

Test label	Specimen	Protocol	Setup	Preload [kN]
HYB-1.1	HYB-1	A	CLT	25.0
HYB-1.2		A	CLT	25.0
HYB-2.1	HYB-2	B	CLT	25.0
HYB-2.2		B	CLT	25.0
HYB-2.3		B	CLT	25.0
HYB-2.4		B	CLT	25.0
HYB-3.1	HYB-3	B	CLT	25.0
HYB-3.2		B	CLT	25.0
HYB-3.3		B	CLT	25.0
HYB-3.4		B	CLT	25.0
HYB_e-1.1	HYB_e-1	B	CLT	25.0
HYB_e-1.2		B	CLT	25.0
HYB_e-1.3		B	CLT	37.5
HYB_e-1.4		B	CLT	37.5
HYB_e-1.5		B	CLT	37.5
HYB_s-1.1	HYB_s-1	B	No CLT	25.0
HYB_s-1.2		B	No CLT	25.0
HYB_s-1.3		B	No CLT	37.5
HYB_s-1.4		B	No CLT	37.5
HYB_s-1.5		B	No CLT	37.5

Protocol A: 1 × 5 mm + 3 × 10–20–30–40–50 mm; 2 mm/s
Protocol B: 1 × 5–10 mm + 3 × 20–40–60–80–100 mm; 2 mm/s.

the prestress variation was not considered in the current experimental setup.

2.4. Overview of the experimental tests

Table 2 summarizes the 20 experimental tests discussed and interpreted in this paper. The first part of the testing campaign (on specimen HYB and HYB_e) was carried out on the main setup that includes the CLT panel. The last 5 tests, on the HYB_s specimen, were carried on the second setup without the CLT specimen following the setup by [55]. The preload value was initially set to 25 kN, than raised to 37.5 kN, in order to achieve an almost 30 kN sliding force. The preload was applied by using the torque method described by the standard EN1090-2 [72] and following the specification of the bolt producer [73]. The labels in Table 2 have been chosen as follows: HYB-i.j, where i indicates the specimen, while j the number of load protocol repetition.

2.5. Experimental results

Fig. 10 displays the force–displacement curves of the tested specimens, while Fig. 11 shows the energy–time curves. The authors superposed in the same plot the outcomes of the load protocol repetitions using different colours and line styles.

The authors measured the prestress provided by the bolts before and after each test using a torque wrench. No significant variation, less than 5%, was observed in the prestress. Therefore, the experimental variation of the slip force, described by a probabilistic model based on the available experimental data, could be reasonably induced by the sole parameters varying in the test: temperature and possible degradation of the shim profile. While a thermocouple tracked the temperature during the tests, the shim layer degradation was not quantified. The authors were limited to observing the degradation by visually comparing the shim layers before and after the test, as remarked in the following sections, see Fig. 12. Thus, the degradation of the shims cannot be included in the probabilistic model calibration.

The inspection of Fig. 10 reveals the following aspects, further investigated in depth in the following sections.

- The tested AFCs exhibit a stable hysteretic response, almost resembling a rectangular-like shape.
- The main differences stands between the specimens with and without the CLT elements. The AFC with the CLT element starts sliding after reaching a certain deformation of the CLT associated with the sliding force of the AFC. Conversely, the AFC without CLT reaches the sliding force with higher pre-sliding stiffness. Therefore, the main consequence of including the CLT element is the reduction of the pre-sliding stiffness due to the screwed connection.
- The sliding force is not constant but evolves during the cycles. It is initially higher than it decreases after multiple cycles.
- The sliding force observed in the first test repetition at the end of the load protocol is lower than the sliding force observed in subsequent test repetitions at the end of the loading protocol.
- The sliding force observed in the first test repetitions at the beginning of the loading protocol is higher than the sliding force observed in the subsequent test repetitions at the beginning of the loading protocol.
- Likely, the sliding force's reduction depends not only on the entire deformation history of the specimen but also on the deformation evolution from the beginning of each test repetition.

The visual inspection of the energy–time curves shows that the dissipated energy rises after each test repetition. The repetition of the same load protocol is associated with a better dissipative performance of the AFC connection. The rate of this enhancement can be different from test to test, as evidenced by comparing specimen HYB-2 and HYB-3. The former has a more significant energy increment after test repetitions than HYB-3. This observation is valid for all the specimens, especially for the HYB_e specimen, where the higher eccentricity is associated with a higher dissipative capacity and a more marked enhancement of the dissipative performance after multiple load protocols.

The enhancement of the AFC performance might depend on the following phenomenon highlighted in the previous paragraphs: The repetition of the load protocols leads to hysteresis curves with higher slip force at higher displacement values.

3. Estimate of the friction coefficient

This section presents a brief introduction on the method followed for estimating the friction coefficient. Then, several plots show the dependence of the friction coefficient on the measured physical variables during the test.

3.1. Theoretical background

The three main assumptions of tribology are [75–77]:

- The total Frictional force (F) is proportional to the applied normal force (N) ($F \propto N$, Amontons' first law)

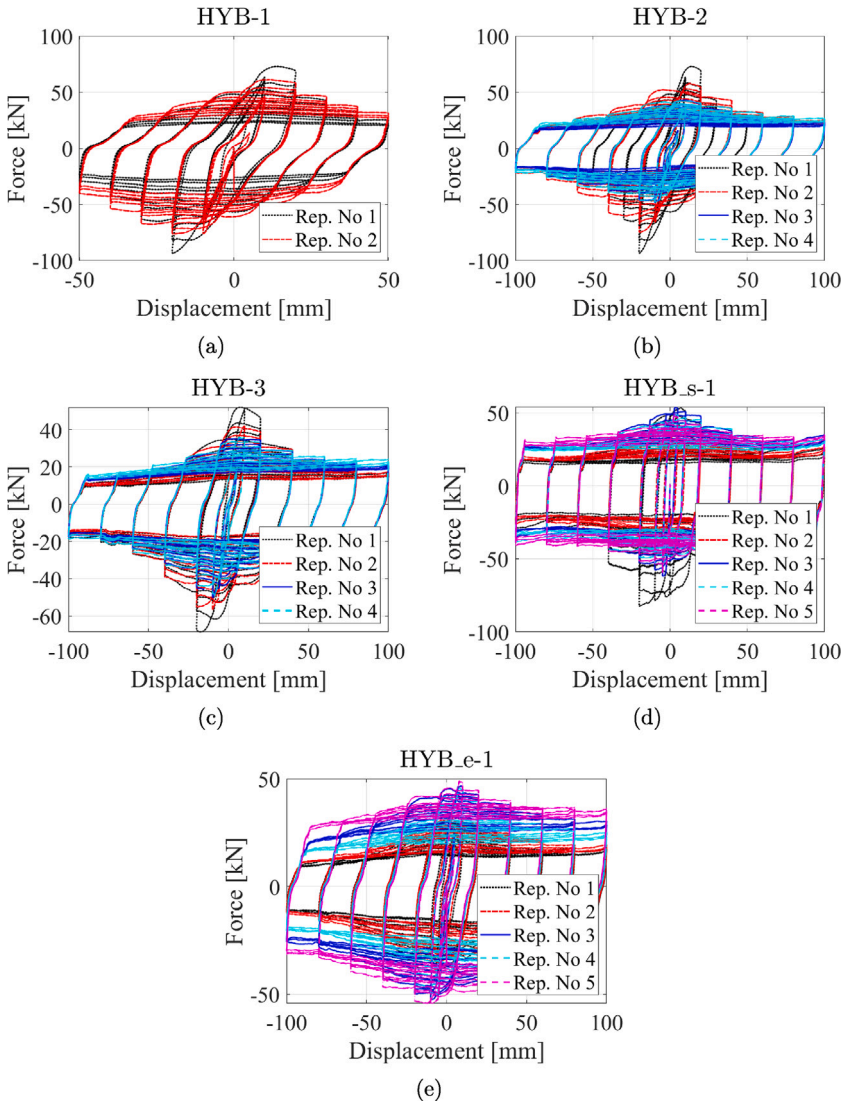

Fig. 10. Force–displacement hysteresis curves of the five tested specimens. The superpositions, obtained with different colours, correspond to identical repetitions (Rep.) of the load protocols. (For interpretation of the references to colour in this figure legend, the reader is referred to the web version of this article.)

- Total frictional force generated is independent of the apparent contact surface area (A) ($F \propto A^0$, Amontons' second law)
- Total frictional force is independent of the relative velocity (V) for very slow sliding velocity ($F \propto V^0$, Coulombs law)

These three theories are generally expressed by the following:

$$F = \mu N \tag{1}$$

where μ is the coefficient of friction, which can vary depending on its state of motion.

However, in the case of dynamic friction, the experimental estimate of the slip force F_{slip} is neither straightforward nor unique. The direct estimation of the dynamic friction coefficient, later referred to as friction coefficient, is sign-dependent, being the ratio between the slip and normal forces. Additionally, the calculation exhibits inconsistent results when using force values due to the velocity inversions during the test. Therefore, Loo et al. [45] adopted a definition of the slip force based on the estimation of the dissipated energy and cumulative displacement. This method does not have the drawbacks of the direct method since it is based on positive and increasing physical quantities. Therefore, the author decided to use the same approach followed by [45]. The dissipated hysteretic energy can be defined as follows:

$$E = \sum_{i=0}^{n} E_i = \sum_{i=0}^{n} \left| \frac{F_{i+1} + F_i}{2} \cdot (\delta_{i+1} - \delta_i) \right| \tag{2}$$

where E is the dissipated energy, E_i the dissipated energy at the $i-$th time step, F_i and δ_i are the force and displacement at the same time step, respectively.

The cumulative distance of travel D is the sum of the displacement time steps:

$$D = \sum_{i=0}^{n} |\delta_{i+1} - \delta_i| \tag{3}$$

The slip force is defined as the work per unit of length:

$$F_{\text{slip}} = \frac{E}{D} \tag{4}$$

The standard deviation is calculated with reference to the F_{slip} value:

$$F_{sd} = \sqrt{\frac{\sum_{i=0}^{n} |F_i - F_{\text{slip}}|^2}{n-1}} \tag{5}$$

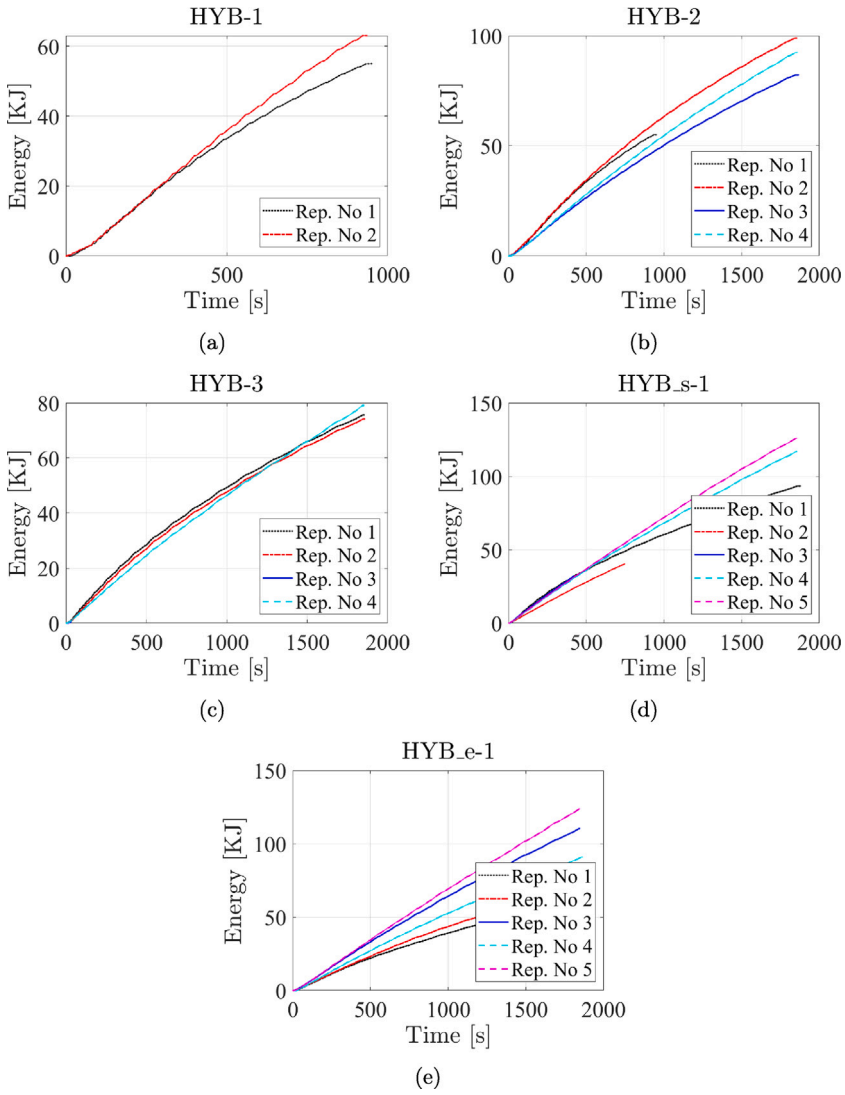

Fig. 11. Dissipated energy–time hysteresis curves of the five tested specimens. The superpositions, obtained with different colours, correspond to identical repetitions (Rep.) of the load protocols. (For interpretation of the references to colour in this figure legend, the reader is referred to the web version of this article.)

Fig. 12. Aluminium shim layers after the tests.

The Coefficient of Variation and the stability parameter λ are calculated as follows:

$$COV = \frac{F_{sd}}{F_{\text{slip}}} \qquad \lambda = \frac{1}{COV} \tag{6}$$

These two values express the loop stability and sliding behaviour nature: a low COV, and thus a high λ value, corresponds to stable performance that resembles the ideal rectangular shape. The experimental friction coefficient μ is calculated as

$$\mu = \frac{F_{\text{slip}}}{n_s n_b F_P} \tag{7}$$

where F_{slip} is the slip force calculated in Eq. (4), n_s is the number of shear surfaces equal to 2, n_b is the number of the preloaded bolts equal to 2, and F_P is the preload force from Table 2.

It must be remarked that the above definition of the friction coefficient cannot be entirely interpreted and understood in light of the Amontons laws. Friction in AFC is not just the product of friction between plates mutually sliding. Therefore, the estimated friction coefficient must be considered a system friction coefficient, representing the entire structural performance.

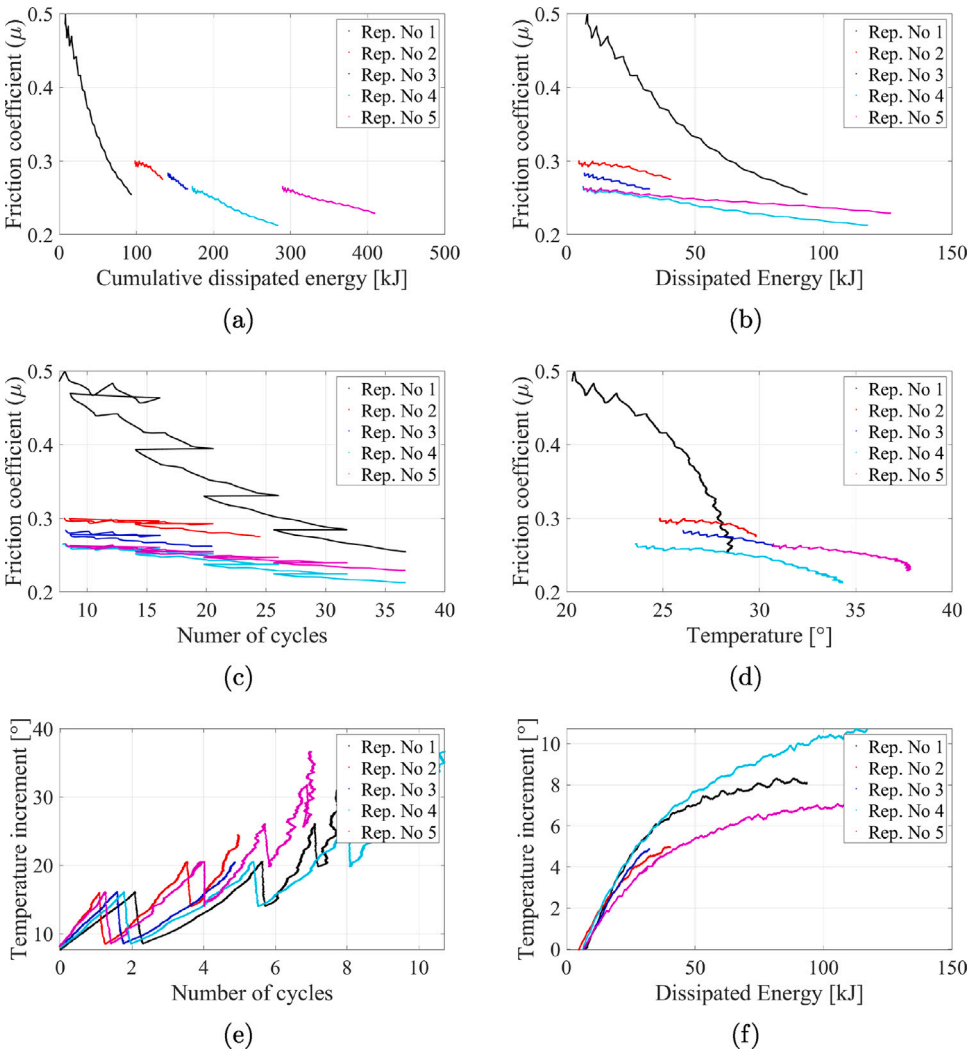

Fig. 13. Dependence of the friction coefficient on the cumulative dissipated energy (a), the dissipated energy estimated from the beginning of the tests (b), the number of cycles (c) and the temperature (d). (e)–(f) show the dependence of the temperature on the number of cycles and the dissipated energy.

3.2. Experimental estimate of the friction coefficient

The previous paragraphs highlighted the meaningful variation of the slip force during the test. Fig. 13 displays a selection of correlations between the estimated friction coefficients and a set of candidate physical quantities, possibly useful for the development of a probabilistic friction model. The plots in Fig. 13 refer to the specimen HYB_s without the CLT element. Fig. 13(a)–(b) are the most significant plots since they show the dependence of the friction coefficient on the dissipated energy calculated from the beginning of the first test and that calculated from the beginning of each test. Fig. 13(a) proves that the friction coefficient depends on the deformation history of the specimen. After an initial friction coefficient close to 0.5, there is an abrupt drop of its value to approximately 0.28 at the end of the test. The friction coefficient corresponding to the beginning of the second test rises to almost 0.3, which is higher than the value estimated at the end of the first load protocol. Still, this increment is minor compared to the significant reduction of the slip force during the first load protocol. Although the variations tend to reduce as the dissipated energy grows, these observations are valid also for the third, fourth and fifth test repetitions.

Fig. 13(b) shows the dependence of the friction coefficient on the dissipated energy calculated from the beginning of each test. These plots evidence a minor dependence of the friction coefficient on the energy dissipated during the tests. The only measured variable increasing during the test is the temperature variation. Therefore, the friction coefficient may depend on both the dissipated energy cumulated from the first test and the temperature variation, proportional to the number of cycles and the dissipated energy during each load protocol, see Fig. 13(e)–(f). The negative friction coefficient–temperature correlation is also manifest in Fig. 13(d), although these effects are more marked in the first load test than the following. Fig. 14 confirms the mutual dependence between the friction coefficient and the temperature by showing for each specimen two curves, one plotting the evolution of the friction coefficient, the other the temperature increment. The reduction of the friction coefficient is generally associated with a temperature increment. Additionally, Fig. 14 reveals that the friction coefficient estimated from the first cycles of the HYB and HYB_e cannot be used for the friction model formulation. As remarked in the previous sections, the AFC has not activated yet in the first cycles due to a lower pre-slip stiffness related to the presence of the CLT specimen. Therefore, the calculation of the friction coefficients excludes the initial points of the loading protocol, where the AFC has not activated yet. The temperature might play a determinant role in affecting the friction coefficient. However, the inclusion of temperature in the friction model would entail a thermodynamic analysis of the AFC during the cyclic response. Besides, the correct estimation of the temperature effect would require experimental tests on the AFC with different initial temperatures for proper calibration. Therefore, the authors developed two probabilistic

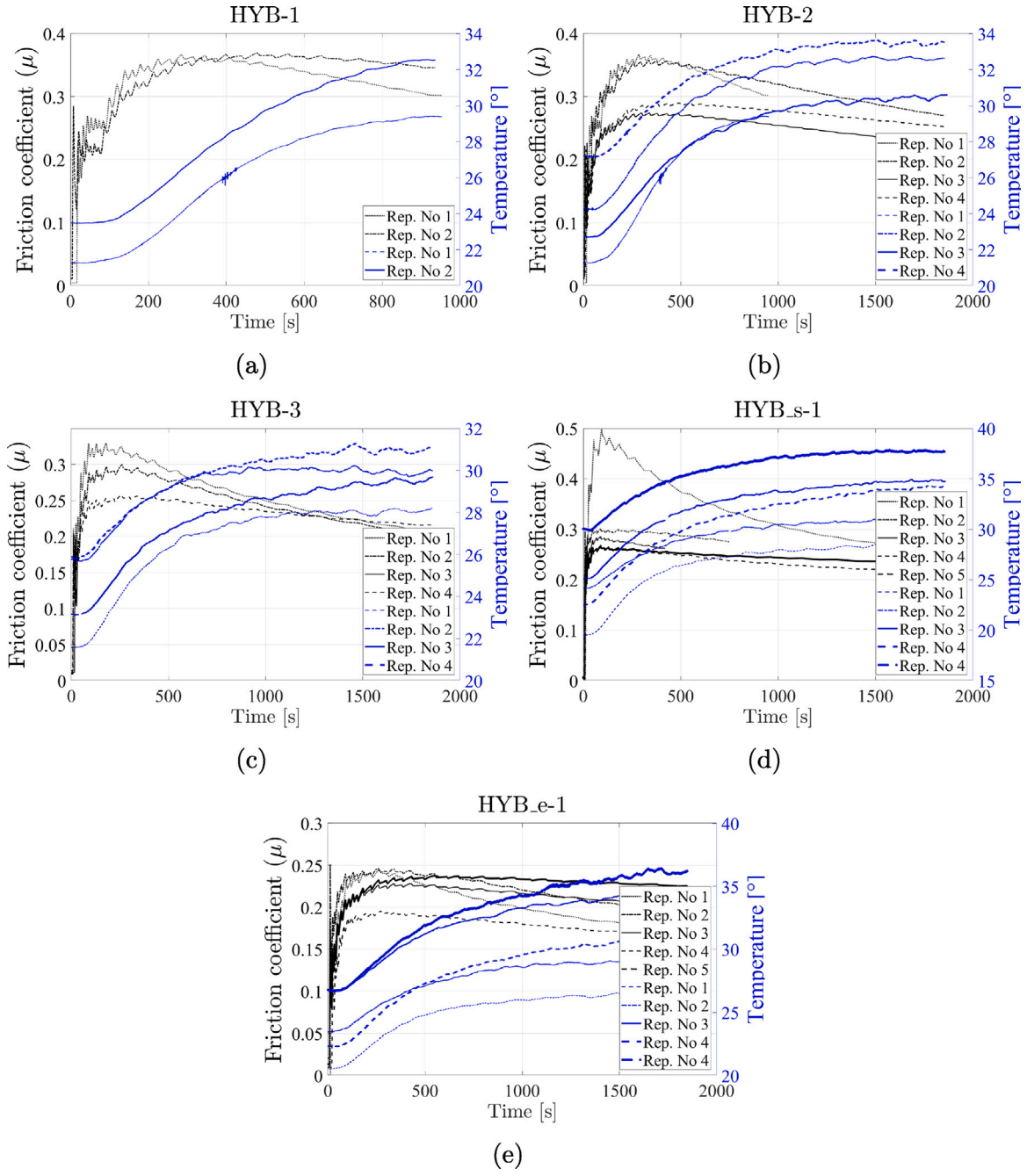

Fig. 14. Evolution of the friction coefficient and the temperature during the loading tests.

friction models. The first, engineering-oriented, depends on the dissipated energy, while the second includes also the measured temperature. The first, engineering-oriented model could be useful for simulating the AFC response in nonlinear dynamic analyses.

4. Probabilistic model of the friction coefficient

The formulation to predict the friction coefficient can be decoupled into two models. The first model defines the dependence between the value of the friction coefficient estimated at the beginning of each cyclic response μ_0 and its value estimated at the beginning of the first cyclic response from the time of the AFC installation $\hat{\mu}_0$. The second model predicts the value of the friction coefficient μ during each cyclic response starting from the value of the friction coefficient estimated at the beginning of the response μ_0. The two models will describe two aspects of the friction coefficient evolution. The first will express the dependence of μ on the deformation history. The second will define its evolution during each cyclic response.

Following [78], the model that relates μ_0 to $\hat{\mu}_0$ is formulated as

$$\log\left(\mu_0\right) = \log\left(\hat{\mu}_0\right) + \gamma_1\left(\epsilon_p\right) + \sigma_1\varepsilon \tag{8}$$

where ϵ_p is the dissipated energy accumulated from the past loading tests of the specimen up to the beginning of the cyclic response to be simulated and $\sigma_1\varepsilon$ is the model error, with σ_1 model standard deviation and ε normally distributed random variable. The logarithm is used as variance stabilizing transformation [79].

The correction term $\gamma_1\left(\hat{\epsilon_p}\right)$ is constructed as a polynomial function of ϵ_p. The relevant terms in the polynomial function are selected using the procedure followed in [78]. The selection process (i.e., the removal of explanatory functions from the initial model [80]) stops after a

Table 3
Posterior statistics of $\boldsymbol{\Theta}$.

$\boldsymbol{\Theta}$	Mean	Stand. dev.	Correlation coefficients							
			θ_1	σ_1	θ_2	θ_3	θ_4	θ_5	θ_6	σ_2
θ_1	$-3.21 \cdot 10^{-2}$	$4.10 \cdot 10^{-3}$	1.00	–						
σ_1	$1.52 \cdot 10^{-1}$	$3.30 \cdot 10^{-2}$	−0.01	1.00						
θ_2	$-2.19 \cdot 10^{-1}$	$7.43 \cdot 10^{-4}$			1.00	–	–	–	–	–
θ_3	$2.46 \cdot 10^{-1}$	$1.83 \cdot 10^{-3}$			0.70	1.00	–	–	–	–
θ_4	$1.31 \cdot 10^{-2}$	$2.09 \cdot 10^{-5}$			−0.99	−0.70	1.00	–	–	–
θ_5	$-1.29 \cdot 10^{-4}$	$2.15 \cdot 10^{-7}$			−0.99	−0.70	0.99	1.00	–	–
θ_6	$1.07 \cdot 10^{-4}$	$2.33 \cdot 10^{-9}$			0.99	0.70	−0.99	−0.99	1.00	–
σ_2	$7.01 \cdot 10^{-2}$	$1.77 \cdot 10^{-4}$			0.70	0.67	−0.70	−0.70	0.70	1.00

Table 4
Posterior statistics of $\boldsymbol{\Theta}$.

$\boldsymbol{\Theta}$	Mean	Stand. dev.	Correlation coefficients								
			θ_6	θ_7	θ_8	θ_9	θ_{10}	θ_{11}	θ_{12}	θ_{13}	σ_3
θ_6	$-1.17 \cdot 10^{0}$	$2.12 \cdot 10^{-3}$	1.00	–	–	–	–	–	–	–	–
θ_7	$2.34 \cdot 10^{-2}$	$4.12 \cdot 10^{-4}$	0.18	1.00	–	–	–	–	–	–	–
θ_8	$-7.53 \cdot 10^{-3}$	$8.00 \cdot 10^{-6}$	−0.95	0.12	1.00	–	–	–	–	–	–
θ_9	$-4.77 \cdot 10^{-3}$	$7.00 \cdot 10^{-5}$	−0.79	0.46	0.94	1.00	–	–	–	–	–
θ_{10}	$4.08 \cdot 10^{-5}$	$3.65 \cdot 10^{-7}$	0.74	−0.53	−0.91	−0.99	1.00	–	–	–	–
θ_{11}	$-1.42 \cdot 10^{-7}$	$7.95 \cdot 10^{-10}$	−0.73	0.54	0.90	0.99	−0.99	1.00	–	–	–
θ_{12}	$2.93 \cdot 10^{-9}$	$7.32 \cdot 10^{-12}$	0.95	−0.14	−0.99	−0.94	0.91	−0.91	1.00	–	–
θ_{13}	$4.05 \cdot 10^{-2}$	$8.20 \cdot 10^{-5}$	0.84	−0.38	−0.96	−0.99	0.98	−0.98	0.96	1.00	–
σ_3	$5.53 \cdot 10^{-2}$	$3.21 \cdot 10^{-3}$	−0.13	0.91	0.40	0.68	−0.73	0.74	−0.42	−0.62	1.00

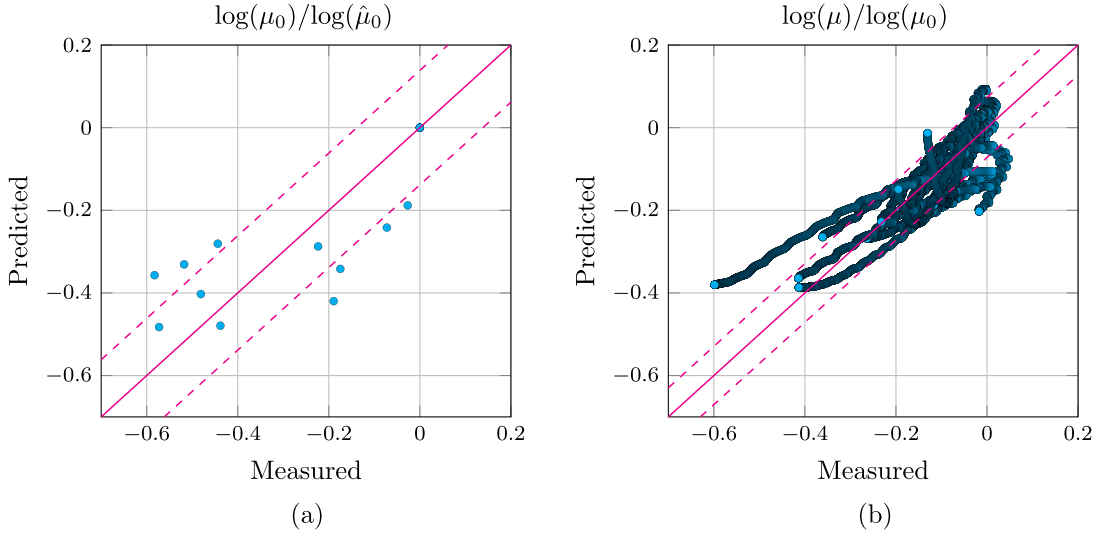

Fig. 15. Predicted capacity versus measured values of the $\log(\mu_0)/\log(\hat{\mu}_0)$ (a) and $\log(\mu)/\log(\mu_0)$ (b).

cumulative increase of the model standard deviation greater than 5% that would lead to an excessive loss of accuracy. Although the number of terms in a probabilistic model is often selected in order to balance accuracy and ease of use, in this case, given the limited amount of data available for the calibration, the number of terms is limited to avoid possible over-fitting of the data.

The model for μ is formally similar and can be written as

$$\log(\mu) = \log(\mu_0) + \gamma_2(\epsilon_p, \epsilon_d, \hat{\mu}_0) + \sigma_2\varepsilon \tag{9}$$

with ϵ_d dissipated energy estimated from the beginning of the current load test, without the contributions related to the past deformation history. Among the explanatory functions considered for γ_2 there are $\hat{\mu}_0$ and powers of e_p and e_d up to the fourth order. Increasing the order of the powers of e_p and e_d above the fourth is avoided because it would lead to a limited increase in accuracy but would also result in an impractical and less manageable model. The models resulting from the selection processes read

$$\log(\mu_0) = \log(\hat{\mu}_0) + \theta_1 {e_p}^{\frac{1}{2}} + \sigma_1\varepsilon \tag{10}$$

and

$$\log(\mu) = \log(\mu_0) + \theta_2 + \theta_3\hat{\mu}_0 + \theta_4 {\epsilon_p}^{\frac{1}{2}} + \theta_5 {\epsilon_d}^2 + \theta_6 {\epsilon_d}^3 + \sigma_2\varepsilon \tag{11}$$

Both models are calibrated with a Bayesian approach following [81]. For all models, the calibration is performed at each stage of the model selection process with the STAN package of the R software [82] that uses a gradient descend method.

Table 3 provides the statistics of the unknown parameters $\boldsymbol{\Theta} = \{\boldsymbol{\theta}, \boldsymbol{\Sigma}\}$, with $\boldsymbol{\theta} = \{\theta_1 \ldots \theta_5\}$ and $\boldsymbol{\Sigma} = \{\sigma_1, \sigma_2\}$. The Adjusted R-squared for the two models are Adj-R^2 = 0.8287 for the model of $\log(\mu_0)$ and Adj-R^2 = 0.7217 for the model of $\log(\mu)$. Fig. 15(a) and (b) show the predicted versus measured values of the ratios $\log(\mu_0)/\log(\hat{\mu}_0)$ and $\log(\mu)/\log(\mu_0)$, respectively. The closer the data points are to the 1:1 lines (i.e., the continuous lines in the figure), the more accurate are the predictions. The two figures also show the region within one standard deviation of the median value (i.e., the region between the dashed lines). From Fig. 15(b), it is possible to recognize data from different load tests. The predictions related to some of them exhibit a limited bias

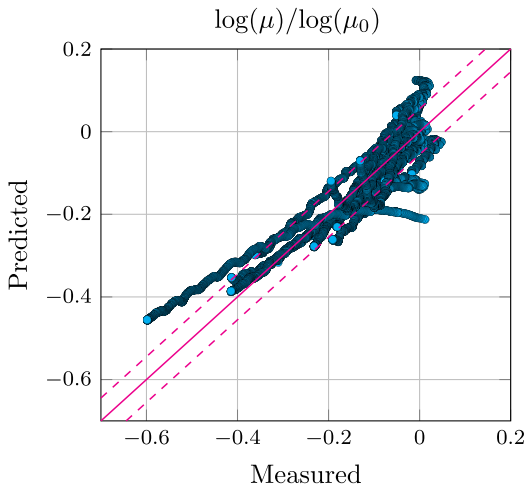

Fig. 16. Predicted capacity versus measured values of the ratio $\log(\mu)/\log(\mu_0)$ when T is included among the explanatory functions.

that may depends on features that are not captured by the explanatory functions considered in the model selection. A prediction for μ can be obtained combining Eqs. (10) and (11) as

$$\mu = \hat{\mu_0} e^{\theta_2+\theta_3\hat{\mu}_0+(\theta_1+\theta_4)\epsilon_p^{\frac{1}{2}}+\theta_5{\epsilon_d}^2+\theta_6{\epsilon_d}^3+\sigma_t\epsilon} \tag{12}$$

where $\sigma_t = ({\sigma_1}^2+{\sigma_2}^2)^{1/2}$. To understand if the temperature can be used as a predictor for the values of μ, the temperature measured during the load test, T, is added into the set of the explanatory functions used to find the correction term for $\log(\mu)$, i.e., $\gamma_2 = \gamma_2(\epsilon_p, \epsilon_d, \hat{\mu}_0, T)$. In this case, the inclusion of T among the explanatory function change the selection process, and T is selected among the significant explanatory functions. The modified model for $\log(\mu)$ has the form

$$\log(\mu) = \log(\mu_0) + \theta_6 + \theta_7\epsilon_p^{\frac{1}{2}} + \theta_8\epsilon_p + \theta_9{\epsilon_p}^2 + \theta_{10}{\epsilon_d}^3 + \theta_{11}\epsilon_d + \theta_{12}{\epsilon_d}^4 + \theta_{13}T + \sigma_3\epsilon \tag{13}$$

The values of the model parameters resulting from the calibration of such a model are presented in Table 4. Fig. 16 shows the agreement between the recorded and predicted values of μ, obtained using Eq. (13). The predictions improve compared to those shown in Fig. 15(b) and the bias of the predictions seems to reduce. Additionally, the standard deviation of the model error is smaller compared to the model in Eq. (12) and the Adjusted R-squared higher (Adj-R^2 = 0.8267). Although the probabilistic friction model dependent on the dissipated energy exhibits a satisfactory performance with an Adj-R^2 = 0.7217, the inclusion of the temperature as a regressor significantly increases the accuracy of the prediction, leading to an Adj-R^2 = 0.8267. This increased accuracy does not show the causal link between temperature increment and friction coefficient reduction. Instead, the probabilistic friction model provides evidence of the temperature role without clarifying if it is the cause or the effect of the friction coefficient variation.

The experimental results and probabilistic model proved that the proposed structural system based on aluminium shims deserves further improvement to achieve a more stable and reliable hysteretic response. There are several passive devices based on friction pads [35] using composite or rubber-based [36,37] friction plates, Belleville springs [33] or thermal spray coating materials [38] offering a stable hysteretic response. The mentioned solutions allow significant seismic energy dissipation without any remarkable decrease in the sliding force, wear, or instability under repetitive loading

5. Conclusion

This research presents the results of quasi-static cyclic tests on Asymmetric Friction Connections (AFC), serving as dissipating devices

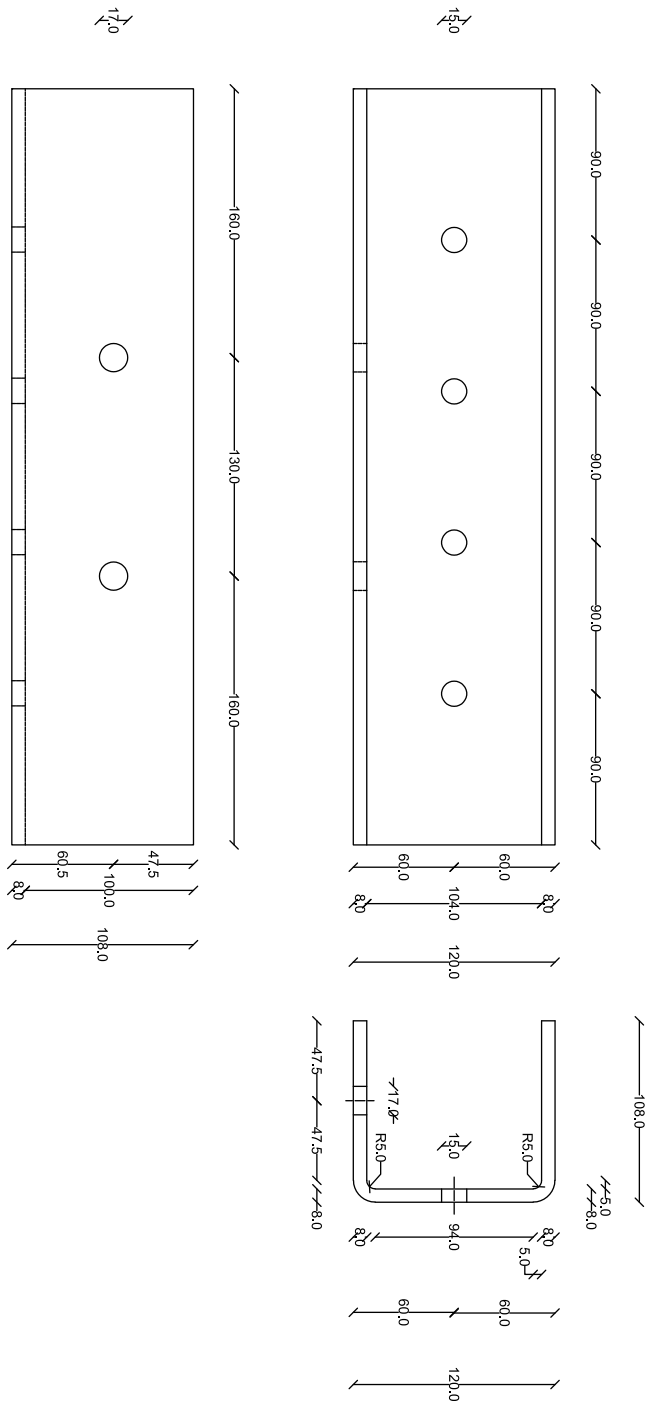

Fig. A.17. Geometric details of the anchor profile of the HYB specimen.

in the e-CLT system [55]. The e-CLT, proposed under the Horizon 2020 research project e-SAFE, is a seismic retrofitting solution for RC frames based on Cross-Laminated timber (CLT) panels and AFCs. The authors carried out multiple repetitions of the same cyclic load protocol to assess the dependence of the aluminium–steel friction coefficient of the tested AFCs on the temperature, the energy dissipated during the test and that dissipated during the past deformation history of the specimen.

The friction coefficient exhibited a significant dependence on both physical quantities. The friction dependence on the dissipated energy during the deformation history might originate from wear phenomena, mainly localized by the bolts, and MPV effects. The mutual sliding between aluminium and steel leads to the abrasive wear of the softer

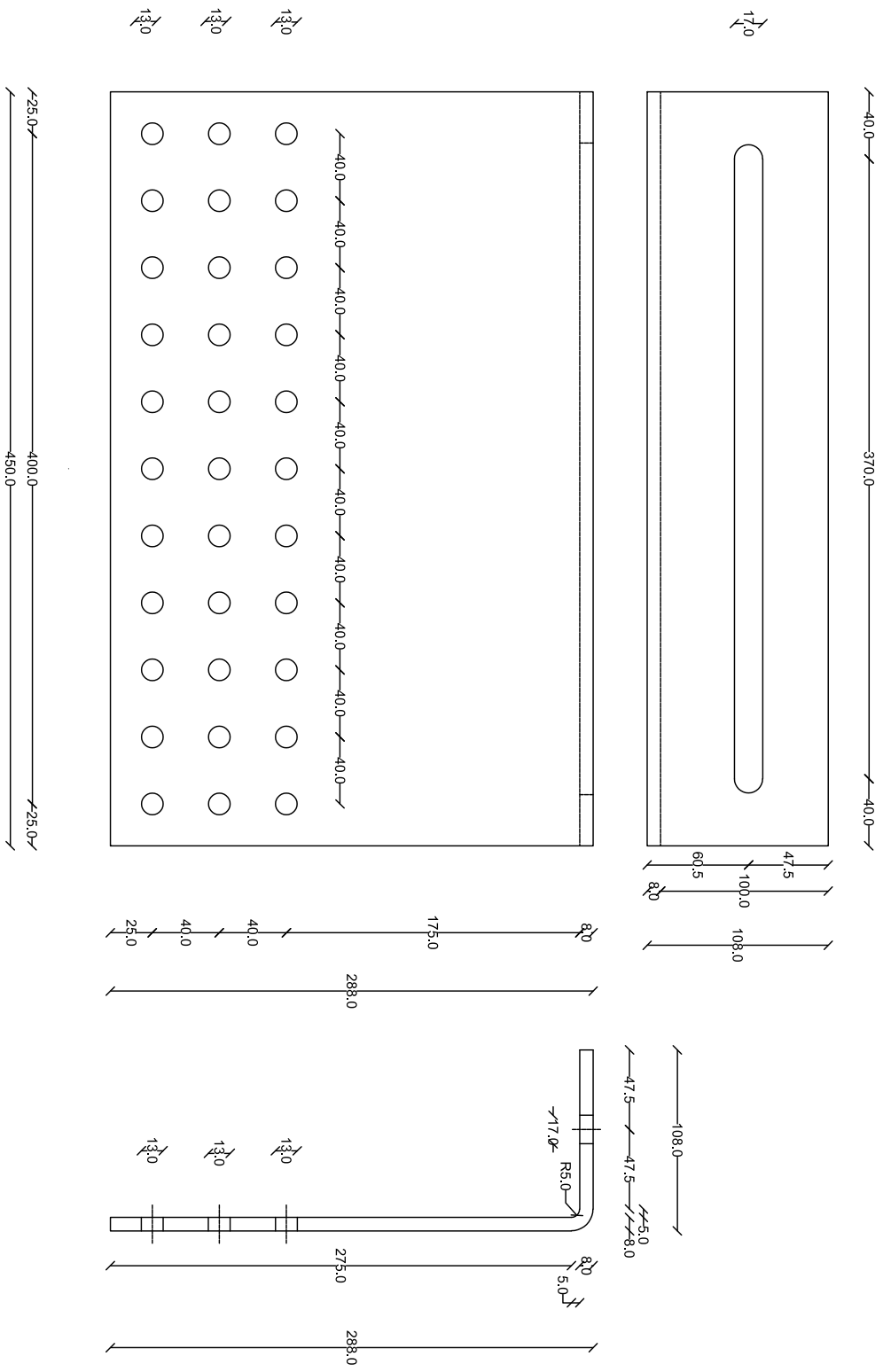

Fig. A.18. Geometric details of the free profile of the HYB specimen.

material (aluminium in the current case) and the reduction of the friction coefficient from nearly 0.5 to 0.2 during the first load protocol. Further repetitions of the load protocols on the same specimen also evidenced a dependence on the dissipated energy cumulated during each test. The physical variable possibly responsible for this phenomenon is the increasing temperature during each loading protocol.

Following the standard semi-physical approach in hysteresis, the authors developed two probabilistic data-driven friction models calibrated from the experimental data using a Bayesian approach. The data-driven model simulates the evolution of friction without distinguishing between the causes of strength degradation's, like MPV interaction, changes in the properties in the sliding surfaces [16,59], and/or prying effects [60,61]. The first engineering-oriented model depends on the dissipated energy, while the second includes the measured temperature as regressor. The first model exhibits a satisfactory performance with an Adj-R^2 = 0.7217. However, the presence of temperature as a

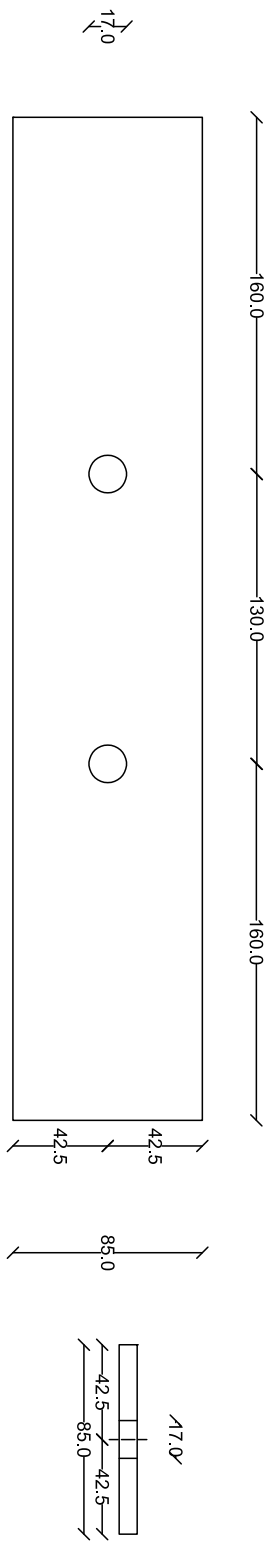

Fig. A.19. Geometric details of the shim layer of the HYB specimen.

regressor significantly increases the accuracy of the prediction, leading to an Adj-R^2 = 0.8267. The higher description capability of the model that includes temperature among the regressors does not show the causal dependence of the friction coefficient reduction on temperature but only the high correlation between the two. Regrettably, the authors do not have multiple tests where the initial temperature of the specimen is varied to rigorously prove the possible dependence of friction on the temperature variation. The first model can predict the friction coefficient in nonlinear analyses of the AFC using a straightforward Coulomb friction model, where the friction coefficient represents an energy-dependent parameter, see [57]. The authors followed a Bayesian approach for calibrating the coefficients of the friction model, which also provides the complete distributions of the model parameters and allows the update of the model with newly available data.

This model can be theoretically extended to different AFCs typologies after proper calibration based on the experimental cyclic response related to multiple load protocols repetitions. Future research efforts, possibly carried out within the Horizon 2020 research grant, will aim to rigorously assess the friction coefficient's dependence on the initial temperature of the specimens.

CRediT authorship contribution statement

Angelo Aloisio: Conceptualization, Methodology, Software, Data curation, Experimental tests, Writing and editing. **Alessandro Contento:** Conceptualization, Methodology, Writing and editing. **Francesco Boggian:** Experimental tests, Conceptualization, Writing and editing. **Roberto Tomasi:** Supervision.

Declaration of competing interest

The authors declare that they have no known competing financial interests or personal relationships that could have appeared to influence the work reported in this paper.

Data availability

Data will be made available on request.

Acknowledgements

The authors would like to thank: Alberto Moretti and the Italian company Adveco s.r.l. for their relevant and continuous support during the prototyping stage and for providing the specimen for the testing campaign; the master student Mathilde Marthinsen for her precious contribution during the testing campaign and the head engineer of NMBU Øyvind Hansen for his continuous support regarding the design and production of the test setup.

Funding

This paper was carried out in the framework of the "Energy and seismic affordable renovation solutions" (e-SAFE) project, which has received funding from the European Union's Horizon 2020 research and innovation programme under grant agreement No. 893135. Neither the Executive Agency for Small and Medium-sized Enterprises (EASME) nor the European Commission is in any way responsible for any use that may be made of the information it contains.

Appendix. Executive drawings of the HYB specimens

See Figs. A.17–A.19.

References

[1] Pall AS, Marsh C. Response of friction damped braced frames. J Struct Div 1982;108(6):1313–23.

[2] Pesaresi L, Stender M, Ruffini V, Schwingshackl C. DIC measurement of the kinematics of a friction damper for turbine applications. In: Dynamics of coupled structures, Vol. 4. Springer; 2017, p. 93–101.

[3] Csaba G. Modelling of a microslip friction damper subjected to translation and rotation. In: Turbo expo: power for land, sea, and air, Vol. 78613. American Society of Mechanical Engineers; 1999, V004T03A012.
[4] Venuti W. Energy absorption of high strength bolted connections. Test Rep 1976.
[5] Pall AS, Marsh C. Friction-damped concrete shearwalls. J Proc 1981;78(3):187–93.
[6] Pall AS. Friction devices for aseismic design of buildings. In: 4th Canadian conference on earthquake engineering. 1983, p. 475–84.
[7] Pasquin C, Leboeuf N, Pall RT, Pall A. Friction dampers for seismic rehabilitation of Eaton's building, montreal. In: 13th world conference on earthquake engineering. 2004, p. 1–2.
[8] Chandra R, Masand M, Nandi S, Tripathi C, Pall R, Pall A. Friction-dampers for seismic control of La Gardenia towers south city, Gurgaon, India. In: 12 th world conference on earthquake engineering, Auckland, New Zealand. 2000.
[9] Pall A, Vezina S, Proulx P, Pall R. Friction-dampers for seismic control of Canadian space agency headquarters. Earthq Spect 1993;9(3):547–57.
[10] Wu B, Li H, Lin L, Shan M. Seismic retrofit of a city hall in northeast China with frictional energy dissipators. J Build Struct 1998;19(5):28–36.
[11] Wu B, Zhang J, Williams M, Ou J. Hysteretic behavior of improved pall-typed frictional dampers. Eng Struct 2005;27(8):1258–67.
[12] Filiatrault A, Cherry S. Performance evaluation of friction damped braced steel frames under simulated earthquake loads. Earthq Spect 1987;3(1):57–78.
[13] Fitzgerald T, Anagnos T, Goodson M, Zsutty T. Slotted bolted connections in aseismic design for concentrically braced connections. Earthq Spect 1989;5(2):383–91.
[14] Latour M, Rizzano G, Santiago A, da Silva LS. Experimental response of a low-yielding, self-centering, rocking column base joint with friction dampers. Soil Dyn Earthq Eng 2019;116:580–92.
[15] Loo WY, Quenneville P, Chouw N. A new type of symmetric slip-friction connector. J Construct Steel Res 2014;94:11–22.
[16] Clifton GC. Semi-rigid joints for moment-resisting steel framed seismic-resisting systems (Ph.D. thesis), Auckland: ResearchSpace@ Auckland; 2005.
[17] Khoo H-H, Clifton C, MacRae G, Zhou H, Ramhormozian S. Proposed design models for the asymmetric friction connection. Earthq Eng Struct Dyn 2015;44(8):1309–24.
[18] Khoo H-H, Clifton C, Butterworth J, MacRae G, Ferguson G. Influence of steel shim hardness on the sliding hinge joint performance. J Construct Steel Res 2012;72:119–29.
[19] Grigorian CE. Energy dissipation with slotted bolted connections (Ph.D. thesis), Berkeley: University of California, Berkeley; 1994.
[20] Mackinven H. Sliding hinge joint for steel moment frames experimental testing. Unpublished ENCI493 project report, Department of Civil Engineering; 2006.
[21] Ramhormozian S, Clifton G, English S, Fredheim S, Beskhyroun S, Macrae G. Dynamic performance analysis and system identification (SI) of a low damage multi-storey structural steel building under two moderately severe earthquake events using structural health monitoring (SHM) data. In: Proceedings of the NZSEE annual technical conference, Auckland, New Zealand. 2018, p. 13–5.
[22] Ramhormozian S, Clifton C, Gledhill S, Muller M. The optimised sliding hinge joint (OSHJ): Design, detail, and implementation in practice. 2021.
[23] Ramhormozian S, Clifton C, Gledhill S. The optimised sliding hinge joint (OSHJ): Overview and first application to a project. In: International conference on the behaviour of steel structures in seismic areas. Springer; 2022, p. 837–43.
[24] MacRae GA, Clifton GC, Mackinven H, Mago N, Butterworth J, Pampanin S. The sliding hinge joint moment connection. Bull N Z Soc Earthq Eng 2010;43(3):202–12.
[25] Yeung S, Zhou H, Khoo H, Clifton G, MacRae G. Sliding shear capacities of the asymmetric friction connection. In: 2013 NZSEE conference, April. 2013, p. 26–8.
[26] Chanchi Golondrino JC, MacRae GA, Chase JG, Rodgers GW, Clifton GC. Hysteretic behaviour of asymmetrical friction connections using brake pads of D3923. Structures 2018;16:164–75.
[27] Chanchi Golondrino JC, MacRae GA, Chase JG, Rodgers GW, Clifton GC. Asymmetric friction connection (AFC) design for seismic energy dissipation. J Construct Steel Res 2019;157:70–81.
[28] Golondrino JCC, MacRae GA, Chase JG, Rodgers GW, Clifton GC. Asymmetric friction connection bolt lever arm effects on hysteretic behaviour. J Earthq Eng 2020;1–22.
[29] Santos AF, Santiago A, Latour M, Rizzano G. Analytical assessment of the friction dampers behaviour under different loading rates. J Construct Steel Res 2019;158:443–59.
[30] Golondrino JC, MacRae G, Clifton C. Behaviour of asymmetrical friction connections using different shim materials. In: Proceedings of the New Zealand society for earthquake engineering conference. 2012.
[31] Jaisee S, Yue F, Ooi YH. A state-of-the-art review on passive friction dampers and their applications. Eng Struct 2021;235:112022.
[32] Ramhormozian S, Clifton GC. Optimised sliding hinge joint (OSHJ): Design and installation guide for a low damage seismic resisting system. 2020.
[33] Ramhormozian S, Clifton GC, MacRae GA, Davet GP, Khoo H-H. Experimental studies on belleville springs use in the sliding hinge joint connection. J Construct Steel Res 2019;159:81–94.
[34] Ramhormozian S, Clifton G, Maetzig S, Cvitanich D, MacRae G. Influence of the asymmetric friction connection (AFC) ply configuration, surface condition, and material on the AFC sliding behaviour. In: New Zealand society for earthquake engineering (NZSEE) annual technical conference, reducing risk raising resilience. Christchurch New Zealand; 2016.
[35] Mualla IH, Belev B. Performance of steel frames with a new friction damper device under earthquake excitation. Eng Struct 2002;24(3):365–71.
[36] Sano T, Shirai K, Suzui Y, Utsumi Y. Loading tests of a brace-type multi-unit friction damper using coned disc springs and numerical assessment of its seismic response control effects. Bull Earthq Eng 2019;17(9):5365–91.
[37] Sano T, Shirai K, Suzui Y, Utsumi Y. Dynamic loading tests and seismic response analysis of a stud-type damper composed of multiple friction units with disc springs. Earthq Eng Struct Dyn 2020;49(13):1259–80.
[38] Cavallaro GF, Francavilla A, Latour M, Piluso V, Rizzano G. Experimental behaviour of innovative thermal spray coating materials for FREEDAM joints. Composites B 2017;115:289–99.
[39] Khoo H-H, Clifton C, Butterworth J, MacRae G. Experimental study of full-scale self-centering sliding hinge joint connections with friction ring springs. J Earthq Eng 2013;17(7):972–97.
[40] Tannert T, Loss C. Contemporary and novel hold-down solutions for mass timber shear walls. Buildings 2022;12(2):202.
[41] Aloisio A, Contento A, Alaggio R, Briseghella B, Fragiacomo M. Probabilistic assessment of a light-timber frame shear wall with variable pinching under repeated earthquakes. J Struct Eng 2022;In press.
[42] Aloisio A, Alaggio R, Fragiacomo M. Equivalent viscous damping of cross-laminated timber structural archetypes. J Struct Eng 2021;147(4):04021012.
[43] Aloisio A, Pelliciari M, Bergami AV, Alaggio R, Briseghella B, Fragiacomo M. Effect of pinching on structural resilience: performance of reinforced concrete and timber structures under repeated cycles. Struct Infrastr Eng 2022;1–17.
[44] Loo WY, Quenneville P, Chouw N. A numerical study of the seismic behaviour of timber shear walls with slip-friction connectors. Eng Struct 2012;34:233–43.
[45] Loo W, Quenneville P, Chouw N. A new type of symmetric slip-friction connector. J Construct Steel Res 2014;94:11–22.
[46] Loo WY, Kun C, Quenneville P, Chouw N. Experimental testing of a rocking timber shear wall with slip-friction connectors. Earthq Eng Struct Dyn 2014;43(11):1621–39.
[47] Loo WY, Quenneville P, Chouw N. Rocking timber structure with slip-friction connectors conceptualized as a plastically deformable hinge within a multistory shear wall. J Struct Eng 2016;142(4):E4015010.
[48] Fitzgerald D, Sinha A, Miller TH, Nairn JA. Axial slip-friction connections for cross-laminated timber. Eng Struct 2021;228:111478.
[49] Fitzgerald D, Miller T, Sinha A, Nairn J. Cross-laminated timber rocking walls with slip-friction connections. Eng Struct 2020;220.
[50] Hashemi A, Zarnani P, Masoudnia R, Quenneville P. Experimental testing of rocking cross-laminated timber walls with resilient slip friction joints. J Struct Eng 2018;144(1):04017180.
[51] Hashemi A, Zarnani P, Masoudnia R, Quenneville P. Seismic resistant rocking coupled walls with innovative resilient slip friction (RSF) joints. J Construct Steel Res 2017;129:215–26.
[52] Hashemi A, Masoudnia R, Quenneville P. A numerical study of coupled timber walls with slip friction damping devices. Constr Build Mater 2016;121:373–85.
[53] Bagheri H, Hashemi A, Yousef-Beik SMM, Zarnani P, Quenneville P. New self-centering tension-only brace using resilient slip-friction joint: Experimental tests and numerical analysis. J Struct Eng 2020;146(10):04020219.
[54] Hashemi A, Quenneville P. Large-scale testing of low damage rocking cross laminated timber (CLT) wall panels with friction dampers. Eng Struct 2020;206:110166.
[55] Boggian F, Tardo C, Aloisio A, Marino EM, Tomasi R. Experimental cyclic response of a novel friction connection for seismic retrofitting of RC buildings with CLT panels. J Struct Eng 2022;148(5):04022040.
[56] Margani G, Evola G, Tardo C, Marino EM. Energy, seismic, and architectural renovation of RC framed buildings with prefabricated timber panels. Sustainability 2020;12(12).
[57] Aloisio A, Boggian F, Tomasi R. Design of a novel seismic retrofitting system for RC structures based on asymmetric friction connections and CLT panels. Eng Struct 2022;254:113807.
[58] Golondrino JCC, MacRae GA, Chase JG, Rodgers GW, Clifton GC. Asymmetric friction connection (AFC) design for seismic energy dissipation. J Construct Steel Res 2019;157:70–81.
[59] Rodgers G, Chase J, Causse R, Chanchi J, MacRae G. Performance and degradation of sliding steel friction connections: Impact of velocity, corrosion coating and shim material. Eng Struct 2017;141:292–302.
[60] Borzouie J, MacRae G, Chase J, Rodgers G, Clifton G. Experimental studies on cyclic performance of column base weak axis aligned asymmetric friction connection. J Construct Steel Res 2015;112:252–62.
[61] Borzouie J, MacRae G, Chase J, Rodgers G, Clifton G. Experimental studies on cyclic performance of column base strong axis–aligned asymmetric friction connections. J Struct Eng 2016;142(1):04015078.
[62] Ramhormozian S, Clifton GC, MacRae GA, Davet GP. Stiffness-based approach for belleville springs use in friction sliding structural connections. J Construct Steel Res 2017;138:340–56.

[63] Ramhormozian S, Clifton GC, Bergen B, White M, Macrae GA. An experimental study on the asymmetric friction connection (AFC) optimum installed bolt tension. In: Proceedings of the NZSEE annual technical conference and 15th world conference on seismic isolation, energy dissipation and active vibration control of structures, Wellington, New Zealand. 2017, p. 27–9.
[64] Ramhormozian S. Enhancement of the sliding hinge joint connection with belleville springs (Ph.D. thesis), ResearchSpace@ Auckland; 2018.
[65] Aloisio A, Pelliciari M, Sirotti S, Boggian F, Tomasi R. Optimization of the structural coupling between RC frames, CLT shear walls and asymmetric friction connections. Bull Earthq Eng 2022;1–26.
[66] Aloisio A, Boggian F, Tomasi R, Fragiacomo M. The role of the hold-down in the capacity model of LTF and CLT shear walls based on the experimental lateral response. Constr Build Mater 2021;289:123046.
[67] Tardo C, Boggian F, Hatletveit M, Marino E, Margani G, Tomasi R. Mechanical characterization of energy dissipation devices in retrofit solution of reinforced concrete frames coupled with solid wood panels. In: Proceedings of the 12th international conference on structural analysis of historical constructions. 2020.
[68] Tardo C, Boggian F, Hatletveit M, Marino E, Margani G, Tomasi R. Mechanical characterization of energy dissipation devices in retrofit solution of reinforced concrete frames coupled with solid wood panels. In: 12th international conference on structural analysis of historical constructions (SAHC 2021). 2021.
[69] EN14399-4. High-strength structural bolting assemblies for preloading - part 4: System HV - hexagon bolt and nut assemblies. 2015.
[70] Rothoblaas. Screws and connectors for wood-carpentry, structures and outdoor. 2022, Accessed: 2022-01-12.
[71] EN15129. Anti-seismic devices. 2018.
[72] EN1090-2. Execution of steel structures and aluminium structures - part 2: Technical requirements for steel structures. 2018.
[73] SBE-Varvit. Structural bolting assemblies EN 14399 preloaded assemblies. 2022, Accessed: 2022-01-12.
[74] Qu Z, Ji X, Shi X, Wang Y, Liu H. Cyclic loading test of steel coupling beams with mid-span friction dampers and RC slabs. Eng Struct 2020;203:109876.
[75] Goedecke A. Transient effects in friction. Springer; 2013.
[76] Halling J. Principles of tribology. Macmillan International Higher Education; 1978.
[77] Persson BN. Sliding friction: physical principles and applications. Springer Science & Business Media; 2013.
[78] Gardoni P, Der Kiureghian A, Mosalam K. Probabilistic capacity models and fragility estimates for RC columns based on experimental observations. ASCE J Eng Mech 2002;128(10):1024–38.
[79] Box GE, Tiao GC. Bayesian inference in statistical analysis. John Wiley & Sons, Ltd; 1992.
[80] Stone CJ. A course in probability and statistics, Vol. 19. Belmont: Duxbury Press; 1996.
[81] Box GE, Cox DR. An analysis of transformations. J R Stat Soc Ser B Stat Methodol 1964;26(2):211–43.
[82] Core Team R. R: A language and environment for statistical computing. Vienna, Austria: R Foundation for Statistical Computing; 2020.